JOURNAL OF COMPUTATIONAL PHYSICS 79, 135–166 (1988)

Numerical Simulation of a Thermally Stratified Shear Layer Using the Vortex Element Method

AHMED F. GHONIEM, GHASSEM HEIDARINEJAD, AND ANANTHA KRISHNAN

Department of Mechanical Engineering, Massachusetts Institute of Technology, Cambridge, Massachusetts 02139

Received January 23, 1987; revised October 5, 1987

In computing the development of an unstable inviscid shear layer, it is found that using a fixed number of vortex elements can lead to large errors due to the strong strain field which develops and acts to distort the original vorticity contours. It is suggested that the vorticity should be redistributed among elements which are arranged in the local principal direction of strain in order to capture this distortion accurately. Mixing within an initially stratified layer, which results from the combined action of convection and diffusion, is computed using a similar scheme to integrate the energy equation. Calculations illustrate the evolution of the temperature profile during the growth of the instability. © 1988 Academic Press, Inc.

I. INTRODUCTION

I.1. *Background*

Numerical simulation of inviscid two-dimensional incompressible flow using vortex discretization of the Euler equations has been discussed extensively in recent literature (Leonard [1], Beale and Majda [2], Hald [3] and Ghoniem and Ng [4]). The method is based on distributing the vorticity field among elements which carry radially-symmetric, compact supports of vorticity (Chorin [5]). By choosing the extent of the support, or the core radius of each element to be larger than the distance of separation between neighboring elements, the fields of individual elements overlap and high order discretization of the vorticity field can be achieved. Vortex elements move with the local flow velocity evaluated at their geometrical centers, which is computed as the summation over the contributions of all elements that exist in the field. The motion of a vortex element does not change its circulation and, in most applications, vortex elements possess invariable core shape and size.

The attraction of these Lagrangian, grid-free methods is that, by construction, computational vortex elements are expected to be, at all times, concentrated around zones of high velocity gradients. When properly exploited, this property endows the scheme with the resolution necessary to study interesting phenomena that arise when molecular diffusion is small relative to convective transport. For instance, at

0021-9991/88 $3.00

high Reynolds numbers, vorticity exists on small patches of the fluid and its suffices to distribute computational elements within these patches and hence avoid wasting labor on zones of very small vorticity. That the elements move to capture large velocity gradients is particularly important in unsteady and nonlinearly unstable flows where the evolution of the instability causes a substantial distortion of the vorticity distribution. Moreover, using a Lagrangian formulation of the equations of motion avoids the convective non-linearity and enables the construction of computational schemes which are explicit in time. The employment of moving Lagrangian grids (Fritts and Boris [6]), or grid-free schemes such as contour dynamics (Zabuski *et al.* [7]), are other successful ways of accomplishing the same goal.

I.2. *Brief Review*

Analysis of the convergence of inviscid vortex methods shows that three factors govern their accuracy: (1) the scheme of discretization of the initial vorticity; (2) the form of the core function; and (3) the ratio of the core radius to the separation between vortex elements (Chorin *et al.* [8], Del-Prete and Hald [9], Hald [3, 10], and Beale and Majda [2, 11, 12]). Results of these analyses have been supported by numerical tests (Nakamura *et al.* [13], Roberts [14], and Perlman [15]). In the following, all three factors are briefly discussed.

To initialize the strength of vortex elements, Del-Prete and Hald [9] used the average vorticity within an area element around the center of the element, while Beale and Majda [2] suggested using the vorticity at the center of the element. Nakamura *et al.* [13] minimized the global error between the continuous and the discrete vorticity distribution to evaluate the latter. Anderson and Greengard [16] proposed the use of a nonuniform mesh to discretize the vorticity field. Using the procedure in [2 or 9], one should expect almost a second-order accuracy for short time if the core function is chosen to be a second-order Gaussian. A fourth-order Gaussian was shown to improve the accuracy. In both cases, a critical parameter is the ratio of the core radius to the distance of separation between the centers of the elements, which must be chosen larger than unity to preserve the accuracy for long time.

As the elements move, their separation exceeds their initial value if a strong strain field arises. This, in effect, decreases the critical ratio of core/separation, leading to deterioration of the accuracy. The fact that large strains cause deterioration in the accuracy of vortex methods has been observed explicitly in analysis, e.g., Leonard [1]. Thus, for most inviscid vortex methods, which are based on using a fixed number of vortex elements with invariant cores, the evolution of large local strains can lead to large errors. For example, a circular patch of vorticity may deform into an elliptical shape with is major axis aligned with the principal direction of strain. If a small fixed number of computational elements is used, they may not be able to accommodate these severe changes. Anderson [17] and Krasny [18], when discretizing non-smooth vorticity, employed a very large core radius so that as vortex elements moved away from each other due to stretch, reasonable overlap could still

be maintained to satisfy the requirements for accuracy. One may also be forced to consider schemes of redistributing the vorticity among a different set of elements under conditions of large strain. Similar schemes have been used in methods of contour dynamics to preserve the accuracy of the integration around the vorticity contours (Zabuski and Overman [19].) Krasny [20], in an independent effort, used a similar procedure in simulating the evolution of a vortex sheet by a desingularized Biot–Savart integral.

Extension of Lagrangian element methods to integrate a scalar conservation equation has been applied to several problems in one dimension (Chorin [21], Ghoniem and Oppenheim [22, 23] and Ghoniem and Sherman [24].) These schemes were based on using the scalar gradient, in analogy to vorticity, in the transport process. Anderson [16, 25] constructed a scheme to solve for a two-dimensional thermal in the inviscid Boussinesq approximation by discretizing the density equation in its vortex form. This was done by casting the equation in gradient form and discretizing the density gradients among elements that could be transported. This scheme, while preserving the advantages of the vortex method, suffers from a major problem: A large strain field, while it may lead to the generation of large gradients, depletes the area of computational elements which are used to transport these gradients.

I.3. *Organization*

In this paper, we apply the inviscid vortex methods to the problem of a temporal shear layer at high Reynolds number. This problem is characterized by a well-defined smooth vorticity field at time zero and has well-documented stability properties. At later times, the shear layer develops into a complicated structure which resembles a turbulent eddy, and a very strong strain field is generated around this eddy. We use the analytical solution of a temporal shear layer to measure the accuracy of the results at the initial stages of development and test the schemes for initializing the vortex elements. At longer times, we observe the effect of the strain field on the accuracy of the computations and suggest ways to cope with it. We then proceed to compute the temperature field as fluids with different temperatures are entrained, stretched, and mixed.

In Section II, the formulation of the vortex method is described and is extended to solve for a flow with a strong strain field. The scheme is applied to compute the evolution of a vorticity layer subject to periodic boundary conditions. The growth of the instability and its effects on the flow field are investigated. In Section III, the concepts of the vortex method are generalized to solve the energy equation and to obtain the temperature profile across the shear layer during its development. The paper ends with conclusions in Section IV.

II. Inviscid Incompressible Flow

II.1. *The Vortex Method*

For an inviscid incompressible flow, the vortex transport equation is

$$\frac{\partial \omega}{\partial t} + \mathbf{u} \cdot \nabla \omega = 0 \tag{1}$$

$$\Delta \psi = -\omega, \tag{2}$$

where $\mathbf{u} = (u, v)$ is the velocity, $\omega = \nabla \times \mathbf{u}$ is the vorticity, $\mathbf{x} = (x, y)$ are the streamwise and cross stream directions, respectively, t is time, $\nabla = (\partial/\partial x, \partial/\partial y)$ and $\Delta = \nabla \cdot \nabla$. Variables are normalized with respect to the appropriate combination of a characteristic velocity and length scale. ψ is the stream function defined so that $u = \partial\psi/\partial y$ and $v = -\partial\psi/\partial x$. The solution of Eq. (1) can be written as

$$\omega(\chi(\mathbf{X}, t), t) = \omega(\mathbf{X}, 0) \tag{3}$$

while χ is governed by

$$\frac{d\chi}{dt} = \mathbf{u}(\chi(\mathbf{X}, t)\, t), \tag{4}$$

where $\chi(\mathbf{X}, 0) = \mathbf{X}$. In the vortex method, the vorticity field $\omega(\mathbf{X}, 0)$ is discretized between elements centered at $\mathbf{X}_i$, $i = 1, ..., N$, so that

$$\omega(\mathbf{x}, 0) = \sum_{i=1}^{N} \Gamma_i f_\delta(\mathbf{x} - \mathbf{X}_i), \tag{5}$$

where $\Gamma_i = \omega_i h^2$ is the circulation of an element of strength ω_i and f_δ is the core function. $f_\delta(\mathbf{x}) = 1/\delta^2 f(r/\delta)$, where $r^2 = x^2 + y^2$, and $\int f_\delta \, d\mathbf{x} = 1$. δ is the core radius, and f_δ is a fast decaying function so that most of the vorticity is concentrated within $r < \delta$. To approximate the initial vorticity distribution accurately, δ should be greater than h, where h is the initial separation between vortex centers. The core function f plays a similar role as interpolating polynomials in finite-difference schemes and base functions in finite-element formulations. By requiring f to be radially symmetric, the approximation in Eq. (5) is at least second order.

Using Eq. (3) and the incompressibility condition, the vorticity distribution at any time is given by

$$\omega(\mathbf{x}, t) = \sum_{i=1}^{N} \Gamma_i f_\delta(\mathbf{x} - \chi_i) \tag{6}$$

where $d\chi_i/dt = \mathbf{u}(\chi_i, t)$ and $\chi_i(\mathbf{X}_i, 0) = \mathbf{X}_i$.

The stream function of a single vortex element is obtained by integrating Eq. (2). Using polar coordinates, for a vortex element placed at $\mathbf{x}=0$, $\partial\psi_\delta/\partial r=-\kappa(r/\delta)/r$, where $\kappa(r)=\int_0^r r'f(r')\,dr'$. Moreover, $u_\theta=-\partial\psi_\delta/\partial r$. The velocity field induced by a distribution of vortex elements, of shape f_δ and strength Γ_i located at $\chi_i(\mathbf{X}_i, t)$ is

$$\mathbf{u}_\omega(\mathbf{x}, t)=\sum_{i=1}^{N}\Gamma_i\mathbf{K}_\delta(\mathbf{x}-\chi_i) \tag{7}$$

where

$$\mathbf{K}_\delta(\mathbf{x})=-\frac{(y,-x)}{r^2}\kappa\left(\frac{r}{\delta}\right). \tag{8}$$

Vortex elements move without changing their circulation (strength) or core shape, at a velocity computed from Eq. (7).

In the calculations, we used mostly a second-order Gaussian core:

$$\begin{aligned} f&=\frac{1}{\pi}e^{-r^2}\\ \kappa&=\frac{1}{2\pi}(1-e^{-r^2}). \end{aligned} \tag{9}$$

When applying the vortex scheme to a flow field with boundary conditions other than $\mathbf{u}(\infty, t)=0$, a potential flow is added to satisfy these conditions. In this work, we perform computations for a periodic shear layer. The velocity field induced by vorticity outside the computational domain $0<x<\lambda$, where λ is the longest wavelength of the perturbation, must be added to $\mathbf{u}_\omega$. These total velocity is

$$\begin{aligned} \mathbf{u}=\sum_{i=1}^{N}\frac{\Gamma_i}{2\pi}\Bigg[&\sum_{j=0}^{\pm1}\frac{(y,-(x+j\lambda))}{((x+j\lambda)^2+y^2)}\exp\left(-\frac{((x+j\lambda)^2+y^2)}{\delta^2}\right)\\ &+\frac{\pi}{\lambda}\frac{(-\sinh(2\pi y/\lambda),\sin(2\pi x/\lambda))}{(\cosh(2\pi y/\lambda)-\cos(2\pi x/\lambda))}\Bigg], \end{aligned} \tag{10}$$

where N is the total number of vortex elements in the computational domain $0<x<\lambda$. Note that since $\delta\ll\lambda$, the effect of the core was included only for the nearest sister vortices.

The initial vorticity distribution across the shear layer can be well represented by a Gaussian curve (with should not be confused with the Gaussian core of individual vortex elements) with a spread 2σ,

$$\Omega(\mathbf{X})=\frac{\Delta U}{\sqrt{\pi}\,\sigma}\exp(-Y^2/\sigma^2), \tag{11a}$$

where ΔU is the velocity difference across the layer and σ is the standard deviation of the Gaussian. The corresponding velocity distribution is

$$U(\mathbf{X}) = \frac{\Delta U}{2} \operatorname{erf}(Y/\sigma), \tag{11b}$$

where $\operatorname{erf}(x) = 2/\sqrt{\pi} \int_0^x \exp(-r^2)\, dr$ is the error function. We take ΔU and σ as the characteristic velocity and length scales of the problem, respectively.

As was pointed out in the Introduction, using either a pointwise discretization, $\omega_i = \Omega(\mathbf{X}_i)$, or an area average value $\omega_i = \int_{hxh} \Omega(\mathbf{X})\, d\mathbf{X}$, where $\mathbf{X}_i$, $i = 1, 2, ..., N$, are the centers of a square mesh of side h, to discretize the vorticity of the shear layer among vortex elements produced a large error in the initial growth of the perturbation. Instead, the following scheme was used,

$$\Omega(\mathbf{X}_i) = \sum_{j=1}^{N} \omega_i h^2 f_\delta(\mathbf{X}_i - \mathbf{X}_j) \tag{12}$$

for $i = 1, 2, ..., N$. The error associated with this distribution was used as a measure of the accuracy of the initial discretization. In all cases, the error $|e_\omega| = \int |\Omega(\mathbf{X}) - \omega(\mathbf{X}, 0)|\, d\mathbf{X} < 10^{-5}$. The error e_ω increased rapidly as δ/h was decreased below one, which is consistent with the result of the convergence theory which shows that the overlap between neighboring elements is necessary for accurate discretization of vorticity. For $\delta/h > 1$, the error was less sensitive to its exact value, until $\delta/h = 1.5$. In the following calculations, we used $\delta/h = 1.1 - 1.4$.

To measure the effect of the accuracy of the initial discretization of vorticity among vortex elements on the flow field for short times, we will use the rate of growth of the perturbation. The growth of the initial perturbation can be characterized by an integral parameter I as

$$I = \int_0^\lambda \int_{-\infty}^{\infty} |u(\mathbf{x}, t) - U(\mathbf{x})|\, d\mathbf{x} \tag{13}$$

which is used in the linear theory analysis of the perturbation.

At $t = 0$, the layer was perturbed by a sinewave with amplitude ε, taken as 0.001λ, 0.01λ, and 0.1λ. In Fig. 1, we compare the growth of the perturbation with the prediction of the linear theory of stability (Michalke [26]) to assess the accuracy of the vortex method for short times. For most of the computations, $\lambda = \lambda^* = 13.2\sigma$, which corresponds to the wave with the maximum growth rate. Equation (4) is integrated using a second-order Heun's method with $\Delta t = 0.1$, and $h = \lambda/44 = 0.3$, and $N(0) = 572$ vortex elements. The figure indicates that for $\varepsilon = 0.01$ and 0.001, the layer behaves linearly and the computed growth rate $\dot{I} = d \ln I/dt = 0.215$ agrees well with the results of the linear theory, $\dot{I} = 0.22$. The latter was computed as the eigenvalue of the linearized Euler equations (Betchov and Criminale [27]). Using $h = \lambda/24$, i.e., $N(0) = 168$, and a second-order time integration scheme, $\dot{I} = 0.23$. For $N = (0) = 572$ and a first-order time integration,

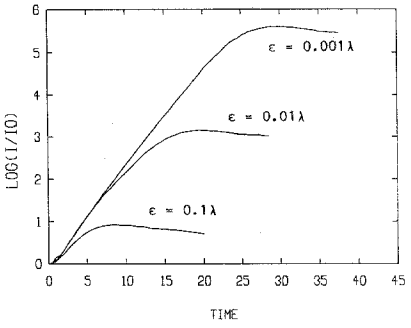

FIG. 1. The growth of the perturbation amplitude I with time for the most unstable case, λ^*, for three values of the initial perturbation $\varepsilon/\lambda = 0.001$, 0.01, and 0.1, showing the linear range and the saturation of the perturbation. Each curve is normalized with respect to the corresponding value of I at $t = 0$.

$\dot{I} = 0.24$. Within this linear stage of development, the maximum distance between neighboring elements in the direction of maximum strain is $\Delta\chi < 1.5h$, i.e., the flow is developing mild stretch. For $\varepsilon = 0.1$, the perturbation leads directly to the nonlinear range.

In Figs. 2, 3, and 4, the vortex elements and their velocity vectors are plotted for $\varepsilon = 0.001\,\lambda$, $0.01\,\lambda$, and $0.1\,\lambda$, respectively. In the first two cases, the end of the linear range corresponds to the beginning of the rollup of the interface, defined here as the line which coincides with $y = 0$ at $t = 0$, and the formation of a spiral center at the midpoint of the wavelength. Concomitantly, the interface starts to stretch near the boundaries of the domain and two saddle points are established at the beginning and end of the wavelength, $x = 0$ and λ. Beyond the linear range, the perturbation continues to grow with more layers rolling around the spiral center and stretching near the saddles. Within this nonlinear range of development, special care must be exercised or the numerical accuracy deteriorates quickly, as exhibited by the evolution of irregular motion near the saddles and the loss of organization of the evolving structure.

II.2. *Effect of Stretch*

The loss of organization, which is associated with the development of strong stretch, illustrates one of the fundamental problems of the vortex method. Vortex elements, which start as cores with radial symmetry, may not properly represent the vorticity field after it has developed strong local strains. As the effective distance, $\Delta\chi$, between neighboring elements increases, the ratio $\delta/\Delta\chi$ (equivalent to δ/h) reaches levels where the vorticity discretization becomes inaccurate. One obvious remedy is to restart the calculations with smaller values of h to allow a larger number of weaker elements to represent the strong distortion. However, that only delays the onset of the crisis at the expense of using more elements at the initial stages when they are not needed. Several remedies may be suggested: (1) utilizing

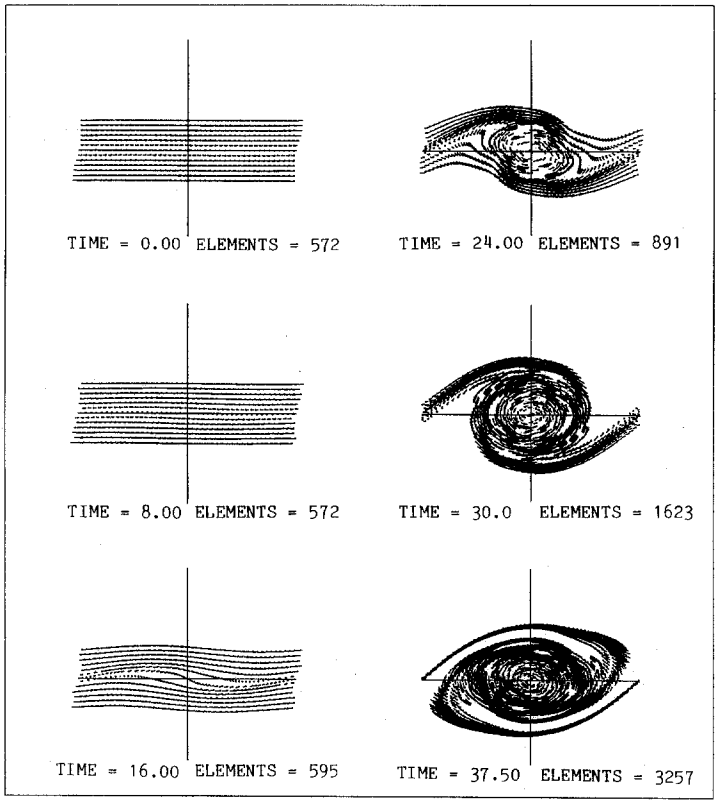

FIG. 2. The location and velocity of the vortex elements during the rollup of a temporal shear. $\lambda = \lambda^*$, with $\varepsilon/\lambda = 0.001$. $N(0) = 572$, $h = 0.3$, $\delta = 0.375$, and $\Delta t = 0.1$.

deformable cores; (2) employing large cores; or (3) using more elements as the distance between the original elements increases.

The first scheme, utilizing deformable cores, depends on assuming that the core structure will become elliptical as stretch develops, with the major axis of each element aligned with the local principal direction of strain. The vorticity distribution within the core must also adapt to he geometrical boundaries of the cores. If elements with constant vorticity within the cores and zero outside, i.e., Rankine vortex elements, are used then these elements will become Kirkchoff vortices which have analytical expressions for the induced velocity field. However, there is an obvious limitation on maintaining one ellipse as a single element if the ratio between its axes exceeds a reasonable value. Thus, this scheme is discarded.

The second scheme, in which one uses large cores, did not yield accurate predictions for the growth rate within the linear range, in accordance with the results of the convergence theory. Moreover, it will fail at the point where $\delta/\Delta\chi < 1$ due to

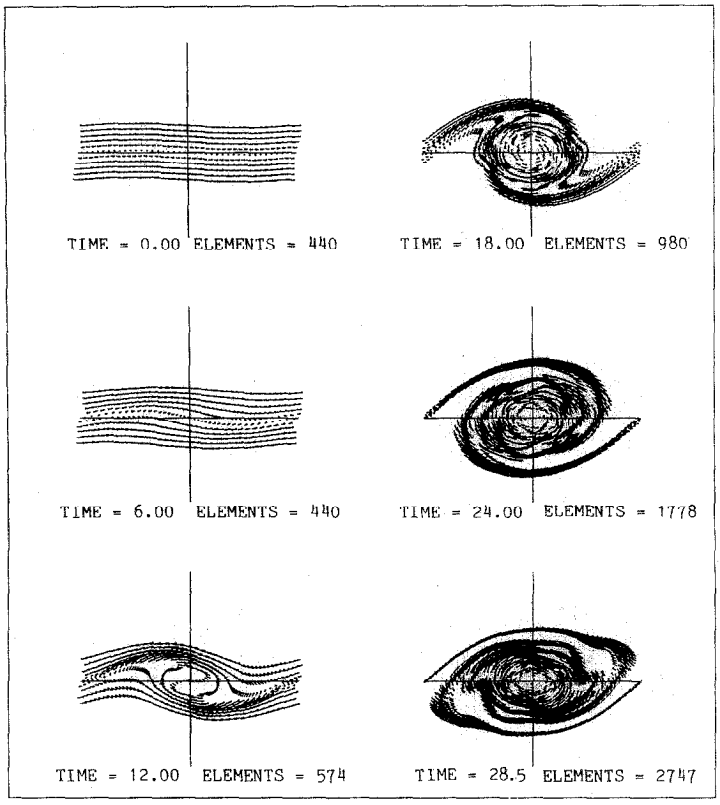

FIG. 3. The location and velocity of the vortex elements. Wavelength is λ^*, and $\varepsilon/\lambda = 0.01$. At $t = 0$, $N = 440$, $h = 0.33$, $\delta = 0.4$, and $\Delta t = 0.1$.

stretch. It does, however, delay the deterioration of accuracy since it maintains a reasonable overlap between neighboring elements for longer times.

The third option, redistributing the vorticity field among an increasing number of elements arranged along the direction of principal direction of strain, is employed here. One monitors the distance between neighboring elements in the direction of maximum positive stretch $\Delta\chi$. If $\Delta\chi > \beta h$, where $1 < \beta < 2$, an extra element is placed halfway between the original elements and the vorticity is redistributed to compute the share of the new element. Ideally, this redistribution should not perturb the existing vorticity field; that is,

$$\omega(\mathbf{x}, t) = \sum_{i=1}^{N} \Gamma_i f_\delta(\mathbf{x} - \boldsymbol{\chi}_i) = \sum_{i=1}^{N+n} \tilde{\Gamma}_i f_\delta(\mathbf{x} - \tilde{\boldsymbol{\chi}}_i), \tag{14}$$

where n is the number of new particles, and a $\tilde{}$ indicates the new value of the strength and location of the vortex elements. Unfortunately, this is a large dense

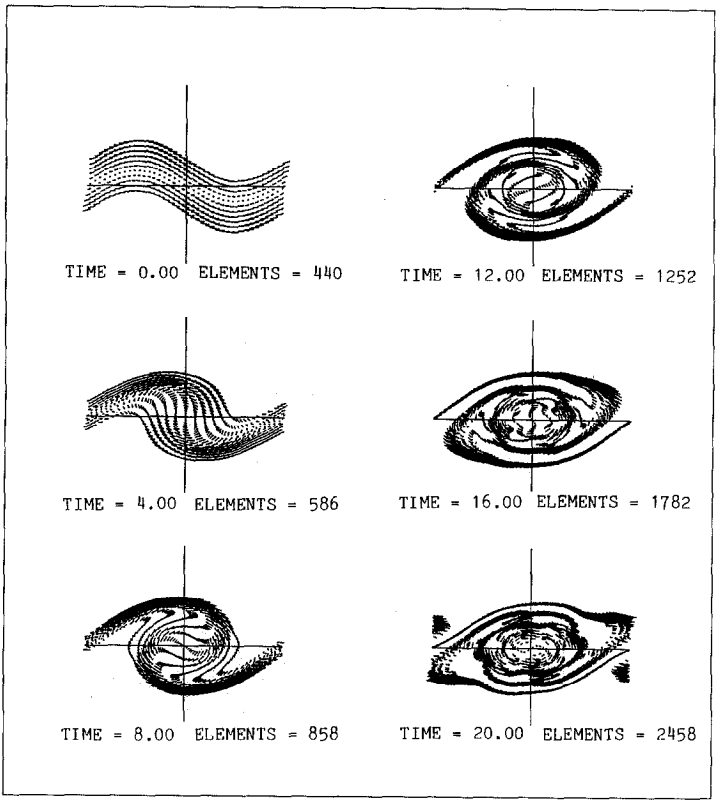

FIG. 4. The location and velocity of the vortex elements for $\lambda = \lambda^*$, and $\varepsilon/\lambda = 0.1$. All the numerical parameters are the same as in Fig. 3.

system of linear equations to be solved every time step. Therefore, its benefit does not warrant the added cost.

A more economical scheme is based on equally distributing the strength of the two original elements among the three elements, i.e., assuming uniform stretch between the two original elements. This amounts to splitting the original vortex dumbbell formed of two vortex discs into three discs when the distance between the centers of the two discs exceeds a threshold, as shown in Fig. 5. To minimize the interpolation errors, the maximum interdistance between neighboring elements is taken as $1.5h$. This will also keep the ratio $\delta/\Delta\chi$ within reasonable limits.

To illustrate the degree of stretch experienced by this flow, we plot the growth of the length of the interface, and the total number of vortex elements, $N(t)$, used to capture this stretch for three perturbations $\varepsilon = 0.001\lambda$, 0.01λ, and 0.1λ in Figs. 6, 7, respectively. Within the linear range the layer is subjected to mild stretch and N remains almost constant. Beyond that, the length of the line grows linearly and N multiplies accordingly. From the plots of the location of vortex elements, we

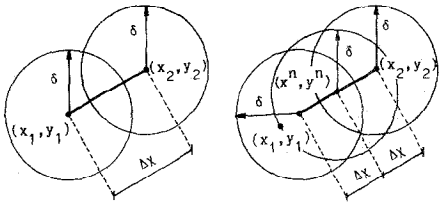

FIG. 5. Schematic diagram showing how the vorticity is redistributed among three elements when the distance between two neighboring elements exceeds a pre-specified value. (x_n, y_n) are the coordinates of the new elements.

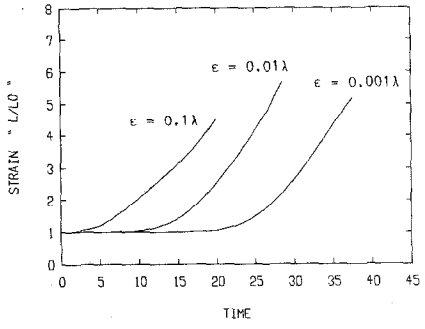

FIG. 6. The total length of the interface, originally at $y=0$, with time for the cases presented in Figs. 2, 3, and 4, normalized with respect to its length at $t=0$.

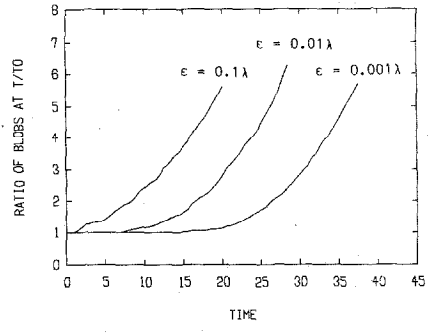

FIG. 7. The number of vortex elements used to represent the vorticity field during rollup for three initial perturbations, normalized with respect to the corresponding value at $t=0$.

noticed that most of the stretch is concentrated around the spiral center and the saddles at the boundaries of the domain.

II.3. *Shear Layer Dynamics*

Figures 1, 2, 3, and 4 reveal that the growth of the perturbation and the development of the eddy structure can be divided into four stages: (1) linear growth; (2) rise to a maximum amplitude; (3) decay to a constant amplitude; and, (4) very slow decrease of amplitude. The first stage has been discussed. The strongest stretch and fastest multiplication of the vortex elements occur during the second stage where an eddy is forming in the middle of the wavelength and two braids are evolving between each two neighboring eddies. During this stage, the core maintains almost a circular configuration and the stretch is concentrated within the braids.

In the third stage, the eddy deforms into an elliptical structure, while the size of the perturbation decreases from its maximum value. This is accompanied by more stretch along the braids and within the core, and a slowdown of the eddy rotation. By the end of this stage, the thickness of the braids at the saddle points has become extremely small. At the final stage, the envelope of the core reaches a dynamic equilibrium, i.e., it does not rotate any more, while its boundaries keep on stretching as the fluid within the eddy starts to move in the main directions of the streams. Although there are signs of that, it is difficult to confirm that the flow has reached a steady state.

The kinetic energy of perturbation $\mathbf{u}' \cdot \mathbf{u}'/2$, where $\mathbf{u}' = \mathbf{u} - U$, and the total kinetic energy in the flow within the computational domain, $\mathbf{u} \cdot \mathbf{u}/2$, are plotted in Figs. 8a and b. The first quantity rises with the growth of the perturbation and the formation of the eddy, then falls with the collapse of the eddy and the return of the fluid to the main streams (Corcos and Sherman [28]). The total kinetic energy is conserved since the flow is inviscid.

Using larger values for h while keeping δ/h the same caused a slight fattening of the core at later times, while the main features of the flow were reproduced almost exactly. A similar modification of the structure is observed when using a first-order time integration scheme or increasing the time step. It was concluded that the errors introduced by using a small number of elements or a low order time integration scheme were numerical-diffusion like errors. We also found that the dependence on the value of h, or the initial number of elements, becomes much less pronounced when the scheme of increasing the number of elements with stretch is employed. Figure 9 shows a qualitative comparison between the experimental results of Roberts *et al.* [29] and the computational results. Here we use a Galilean transformation to compare the experimental results of the spatially developing layer and the computational results of the temporal layer.

The physical parameters that govern the flow field are λ and ε. Results for the rollup of a layer with $\lambda = 10.5 < \lambda^*$ are presented in Figs. 10 and 11, showing the growth of the perturbation and the vorticity field. λ^* is the wavelength of the most unstable perturbation. The computed growth rate $\dot{I} = 0.214$ while the analytical

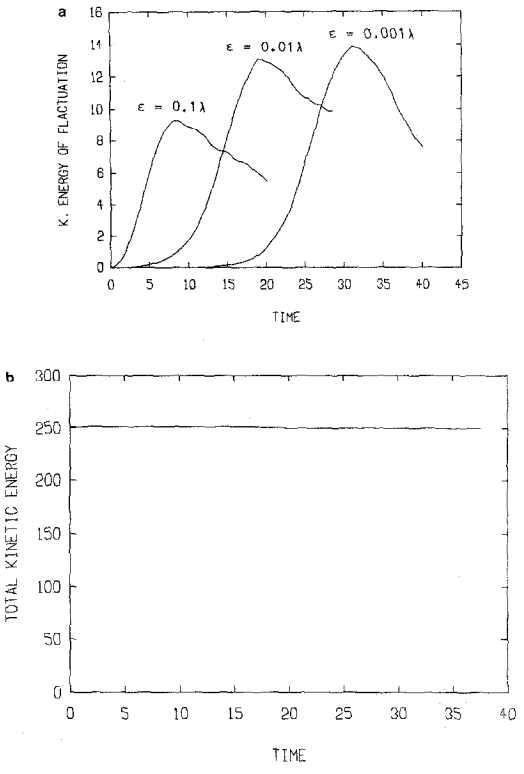

FIG. 8. (a) The total kinetic energy of the perturbation based on the perturbation velocity, $(U(x)-u(x,t))^2$, and (b) The total kinetic energy of the flow, u^2, for $\varepsilon/\lambda = 0.001, 0.01, 0.1$.

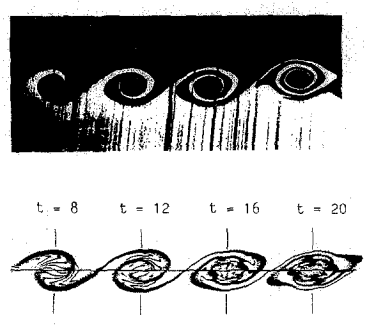

FIG. 9. The evolution of the vorticity field with time, compared with the experimental results of Roberts *et al.* [29] for the spatial development of a small perturbation of a shear layer.

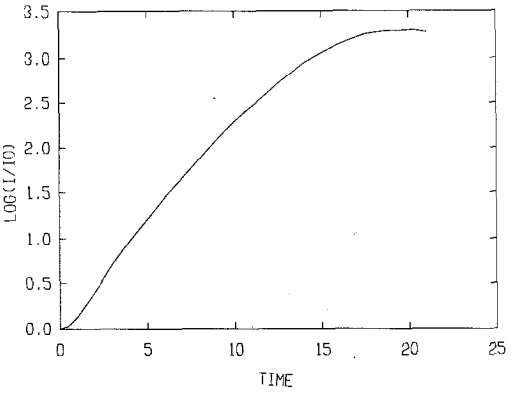

FIG. 10. The growth of the perturbation amplitude for $\lambda = 10.5$, $\varepsilon/\lambda = 0.01$, $N(0) = 455$, $h = 0.3$, $\delta = 0.375$, and $\Delta t = 0.1$.

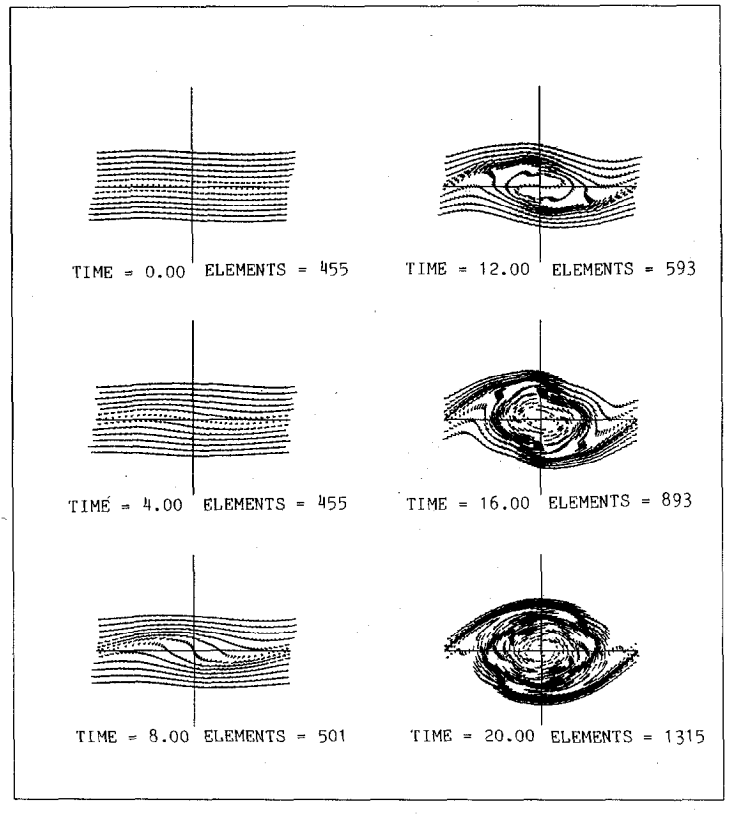

FIG. 11. The location and velocity of the vortex elements used in the calculations of the case shown Fig. 10.

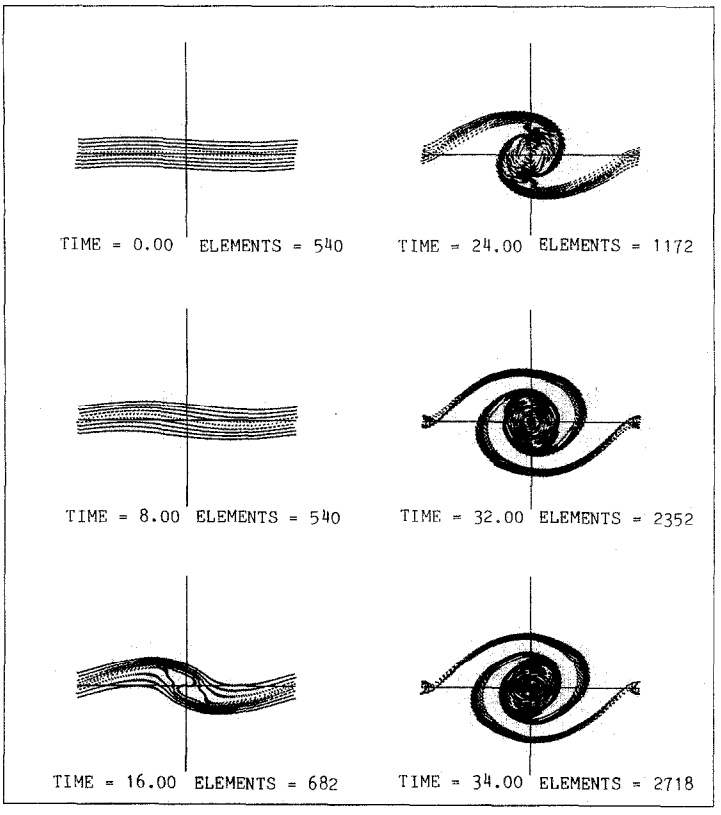

FIG. 12. The vorticity field for $\lambda = 2\lambda^*$, $\varepsilon/\lambda = 0.01$, $N(0) = 540$, $h = 0.44$, $\delta = 0.5$, $\Delta t = 0.1$.

value is 0.208. More vorticity remains in the braids between the eddies which are not strong enough to accomplish the same stretch as in the case of λ^*.

Figures 12 and 13 show results for $\lambda = 2\lambda^*$, with $\varepsilon = 0.01\,\lambda$ and $0.1\,\lambda$, respectively. In the first case, $\dot{I} = 0.18$ while the analytical result is 0.173. The core is smaller and weaker than for the case of λ^* and hence the braids are thicker and maintain more of the original vorticity. At later times, a small scale rollup is obsered near the boundary of the domain due to the instability of the vorticity layer that forms the braids. This rollup occurs only at the fourth stage of development when the mid-section of the braids becomes almost stationary, i.e., when the motion produced by the braids is neutralized. Comparing Figs. 12 and 13, we see that contrary to the most unstable case, the effect of the initial perturbation is more pronounced here in terms of the size and shape of the eddy and the braids. Higher amplitudes of perturbation tend to form a larger core and thinner braids. The ratio between the major and minor axes of the elliptical core increases with ε and small amplitude waves start to appear on the braids.

Figures 14 and 15 show results for $\lambda = 3\lambda^*$ with amplitudes $\varepsilon = 0.01\lambda$, and 0.1λ,

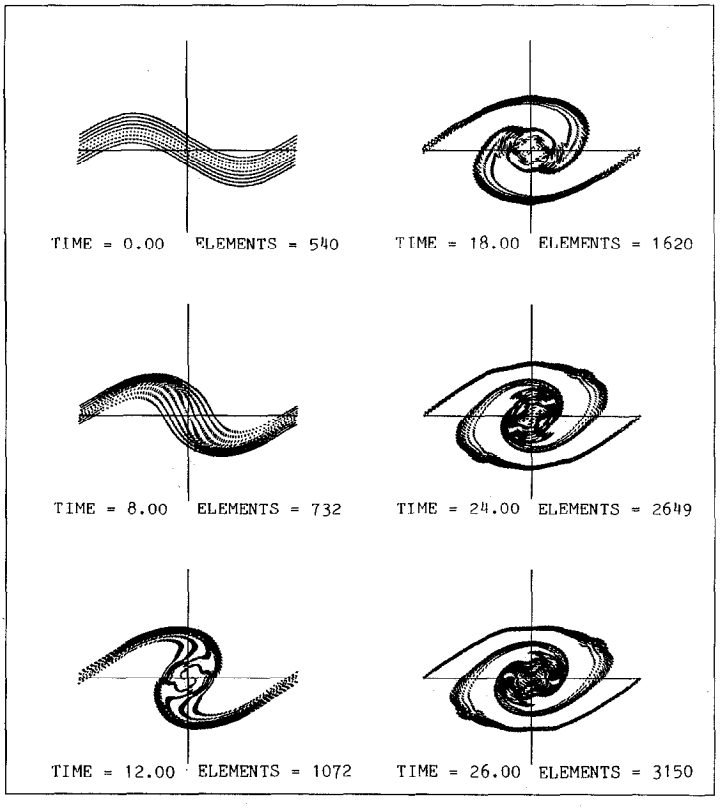

FIG. 13. The vorticity field for $\lambda = 2\lambda^*$, $\varepsilon/\lambda = 0.1$, using the same numerical parameters as in Fig. 12.

respectively. The effect of the amplitude is emphasized further since at larger ε, the core splits into two eddies. This bifurcation phenomenon was observed before by Pozrikidis and Higdon [30]. The braid instability is manifested here by the long waves that appear at the later stages of development of the layer.

With the presence of two perturbation wavelengths, a new process is observed. Figures 16 and 17 depict results for a layer subject to two perturbations superimposed at $t = 0$, at λ^* and $2\lambda^*$ with $\varepsilon = 0.1\lambda^*$ for both perturbations. The results

the end of the second stage and before any substantial elongation of the eddies. The growth of the subharmonic perturbation closely resembles that of the fundamental, as shown in Fig. 17. The eddies continue to deform while they pair until the "vortex fluid" contained within each structure start to rotate around a common center and their original boundaries become indistinguishable. Similar qualitative observations were shown in the computations of Corcos and Sherman [28] and Riley and Metcalfe [31].

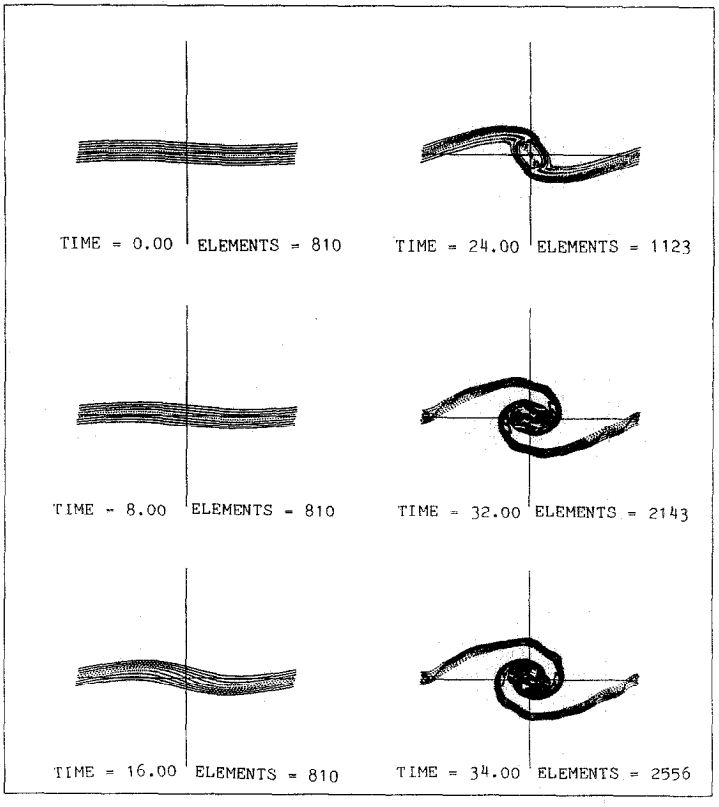

FIG. 14. The vorticity field for $\lambda = 3\lambda^*$, $\varepsilon/\lambda = 0.01$, $N(0) = 818$, and the values of h, δ, and Δt are the same as in Fig. 12.

III. THE TEMPERATURE DISTRIBUTION

III.1. *The Transport Element Method*

In an inviscid incompressible flow, the temperature distribution evolves according to the following form of the conservation of energy:

$$\frac{\partial T}{\partial t} + \mathbf{u} \cdot \nabla T = 0, \tag{15}$$

where T is temperature. This is equivalent to the statement that $T(\chi(\mathbf{X}, t), t) = T(\mathbf{X}, 0)$, where $\chi(\mathbf{X}, 0) = \mathbf{X}$ and $d\chi/dt = \mathbf{u}(\chi, t)$. To solve this equation using a Lagrangian element scheme, we start by introducing the temperature gradient $\mathbf{q} = \nabla T$, where $\mathbf{q} = (p, q)$ is a vector proportional but opposite to the heat flux

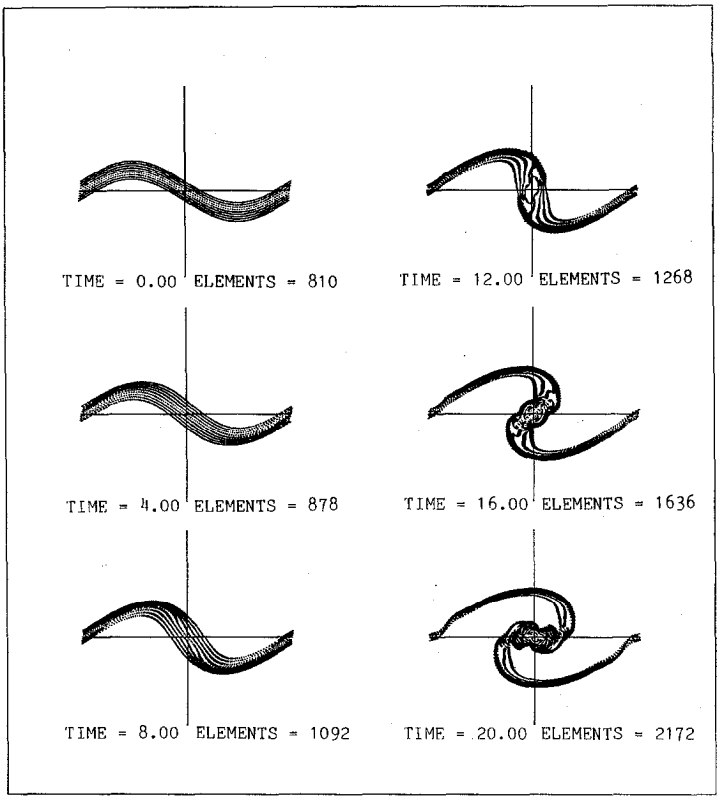

FIG. 15. The vorticity field for $\lambda = 3\lambda^*$, $\varepsilon/ = 0.1$, using the same numerical parameters as in Fig. 14.

vector $-k\mathbf{q}$, k being the thermal conductivity. The transport equation of $\mathbf{q}$ is obtained by taking the gradient of Eq. (15) and rearranging,

$$\frac{\partial \mathbf{q}}{\partial t} + \mathbf{u} \cdot \nabla \mathbf{q} = -\mathbf{q} \cdot \nabla \mathbf{u} - \mathbf{q} \times \boldsymbol{\omega} \tag{16}$$

where $\boldsymbol{\omega} = \omega \mathbf{e}_z$ and $\mathbf{e}_z$ is the unit vector normal to the (x, y) plane. Thus, along a particle path $\chi(\mathbf{X}, t)$, the temperature gradient changes according to the local strain field and turns with the local rotation of the fluid element. Using the vortex method described in the previous section, the velocity gradient may be computed directly from the vorticity distribution as: $\nabla \mathbf{u} = \sum \Gamma_i \nabla \mathbf{K}_\delta(\mathbf{x} - \chi_i) + \nabla \mathbf{u}_p$, where $\mathbf{u}_p$ is the irrotational component of the velocity.

The scheme proceeds in the same way as the vortex algorithm. The initial temperature gradient is discretized among a number of elements located at the centers of a square mesh of side h so that

$$\mathbf{q}(\mathbf{x}, 0) = \sum_{i=1}^{N} \mathbf{q}_i h^2 f_\delta(\mathbf{x} - \mathbf{X}_i), \tag{17}$$

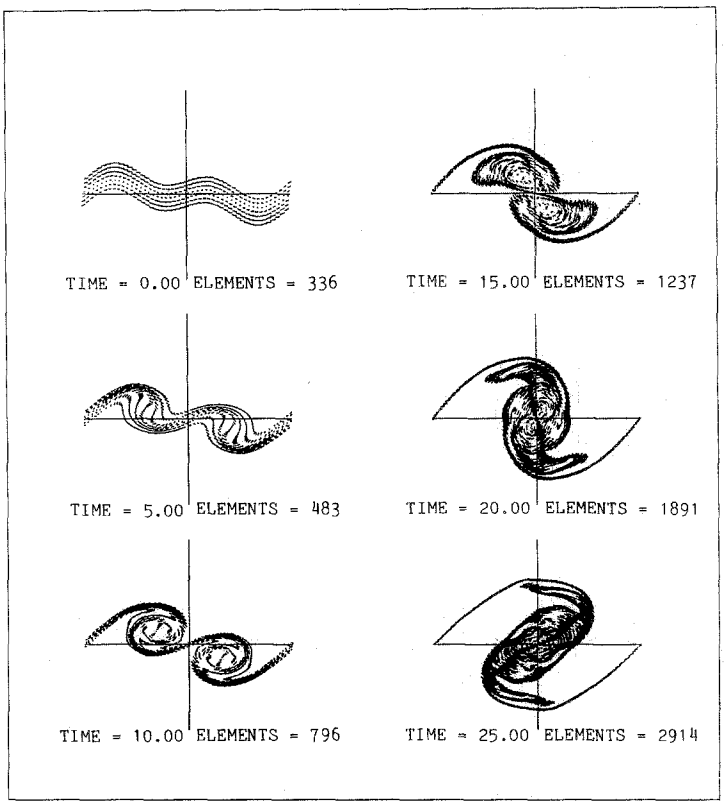

FIG. 16. The location and velocity of the vortex elements for two perturbations, $\lambda_1 = \lambda^*$ and $\lambda_2 = 2\lambda^*$, with $\varepsilon = 0.1\lambda^*$ for both perturbations. $N(0) = 336$, $h = 0.55$, $\delta = 0.6$, and $\Delta t = 0.5$. A fourth-order time integration scheme is used to transport the elements.

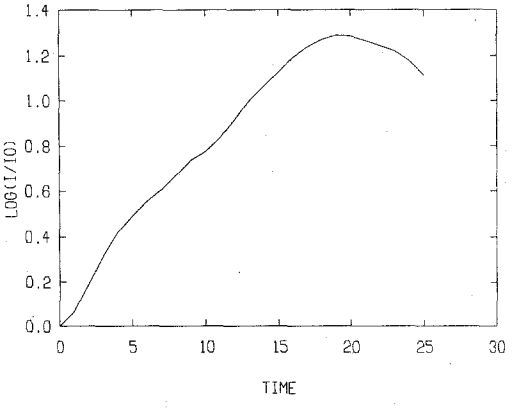

FIG. 17. The total amplitude of the perturbation of the case in Fig. 16.

where $\mathbf{q}(\mathbf{x}, 0)$ is the initial distribution of the temperature gradient, $\mathbf{q} = \nabla T(\mathbf{X}, 0)$. To initialize $\mathbf{q}_i$, a similar procedure to that used in computing the strength of the vortex elements is employed here, i.e., Eq. (12) with $\mathbf{q}$ instead of ω, is solved to find $\mathbf{q}_i(0)$. To update $\mathbf{q}_i(t)$, Eq. (16) is solved in two fractional steps; in the first step, the elements are transported without changing their strength or their core shape or size. In the second step, the strength of the elements is updated according to

$$\frac{d\mathbf{q}_i}{dt} = -\mathbf{q}_i \cdot \nabla \mathbf{u}_i - \mathbf{q}_i \times \boldsymbol{\omega}_i. \tag{18}$$

Thus, a system of ordinary differential equations must be integrated to update the strength of the gradient elements as they move along particle paths. The local gradient at time t is computed from

$$\mathbf{q}(\mathbf{x}, t) = \sum_{i=1}^{N} \mathbf{q}_i(t)\, h^2 f_\delta(\mathbf{x} - \boldsymbol{\chi}_i). \tag{19}$$

The core function f_δ may be different for the vortex elements and the gradient transport elements. In this work, we use the same form for both. The temperature can be calculated by direct integration of the gradient along a determined path. As pointed out by Anderson [17], a convenient expression can be obtained by expressing the temperature as a Poisson integral in the temperature gradient, $T = \int \nabla G(\mathbf{x} - \mathbf{x}') \cdot \nabla T(\mathbf{x} - \mathbf{x}')\, d\mathbf{x}'$. Using Eq. (19) for $\mathbf{q}_i$, we get

$$T(\mathbf{x}, t) = \sum_{i=1}^{N} \mathbf{q}_i(t) \cdot \nabla G_\delta(\mathbf{x} - \boldsymbol{\chi}_i), \tag{20}$$

where

$$\nabla G_\delta = \frac{(x, y)}{r^2} \kappa\left(\frac{r}{\delta}\right)$$

while the relationship between f and κ is as before. This expression is convenient when used in connection with the vortex method since all the functions involved in the summation must be computed for the transport of the vortex elements and with simple programming tricks, the increase in cost can be minimized.

Results obtained for the temperature distribution in the shear layer of Figs. 2, 3, and 4 are shown in Figs. 18, 19, and 20, respectively. At $t = 0$, the temperature distribution is described by an error function, with $T(\mathbf{x}, 0) = 0.5(1 + \text{erf}(Y))$. This choice is motivated by the fact that this is the fundamental solution of the diffusion equation. Therefore, an initial discontinuity in temperature would develop into an error function before the perturbation grows and convection effects become important. The layer is first perturbed by a sinewave by displacing the elements according to $Y = \tilde{Y}(X)$, and then the temperature gradient $\mathbf{Q}(\mathbf{X})$ is computed. The discrete values $\mathbf{q}_i(0)$ are obtained as follows: Since the temperature is constant along the streamlines after the perturbation $Y = \tilde{Y}(X)$, then $T(\mathbf{X}, 0) = \Theta(\mathbf{X}) =$

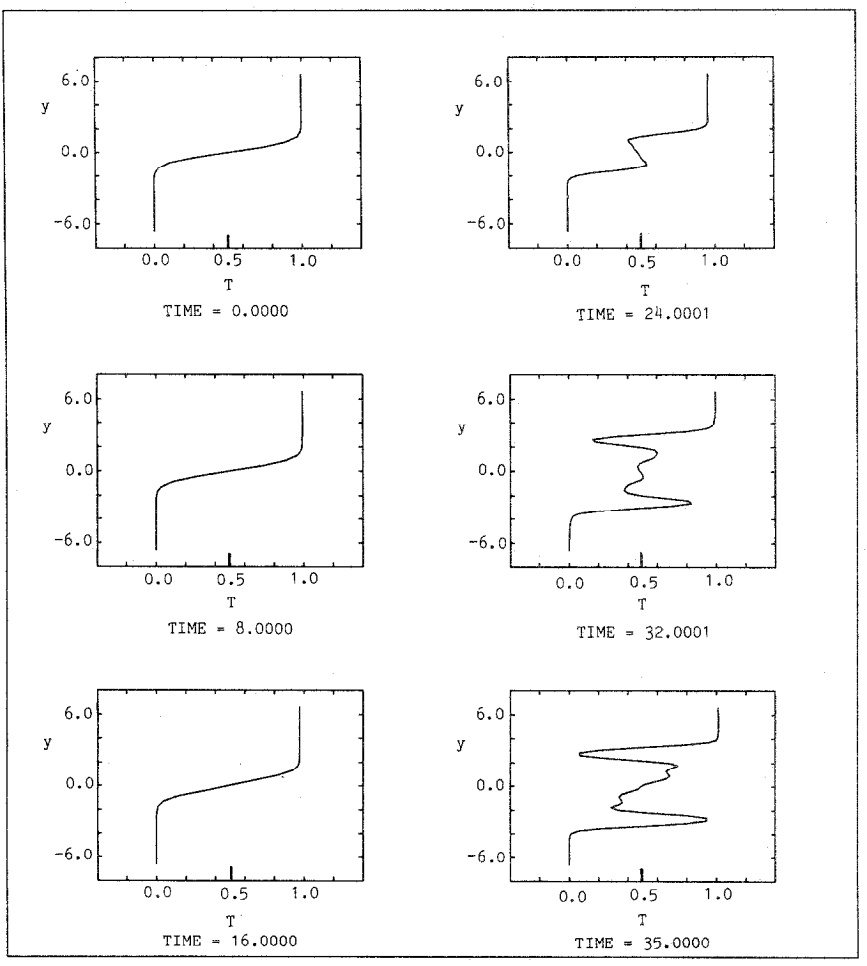

FIG. 18. The temperature distribution across the layer at the center of the core, for λ^* and $\varepsilon/\lambda = 0.001$. The numerical parameters are the same as in Fig. 2.

$0.5(1+\text{erf}(Y-\tilde{Y}(X))$. From this equation we can recover the initial distribution of $P(X,0)$, and $Q(X,0)$ as

$$P(\mathbf{X}) = \frac{\partial \Theta}{\partial X} = -\text{Gau}(Y-\tilde{Y}(X))\frac{d\tilde{Y}}{dX}$$
$$Q(\mathbf{X}) = \frac{\partial \Theta}{\partial Y} = \text{Gau}(Y-\tilde{Y}(X)), \tag{21}$$

where Gau is a Gaussian similar to Eq. (11a). These expressions are then used in Eq. (17) to compute $\mathbf{q}_i$. The values of $\mathbf{q}_i(0)$ were initialized one column at a time, i.e., for fixed values of X, to avoid solving N^2 simultaneous equations, and instead

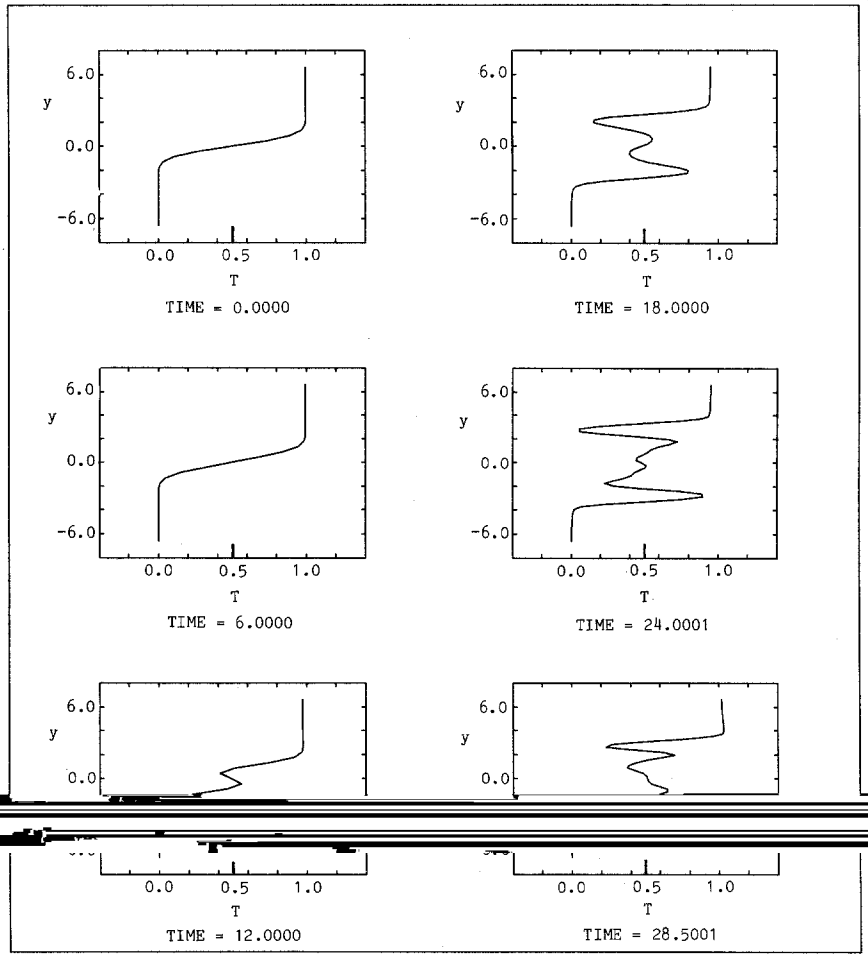

FIG. 19. The temperature distribution across the layer at the center of the domain for λ^* and $\varepsilon/\lambda = 0.01$. The numerical parameters are the same as in Fig. 3.

solve N_X of N_Y simultaneous equations. The error associated with this approximation was very small since the perturbation was kept at a low value.

In the computations, we used the same particles to transport vortex elements and elements of the temperature gradient. This represents a substantial saving since the kernel functions appearing in the expressions of the velocity, velocity gradients, and temperature can be computed all at once and the velocity is computed only for one set of elements.

III.2. *Entrainment in a Shear Layer*

To quantify the overall change in the temperature distribution, we define a quantity Y, similar to the growth I, as

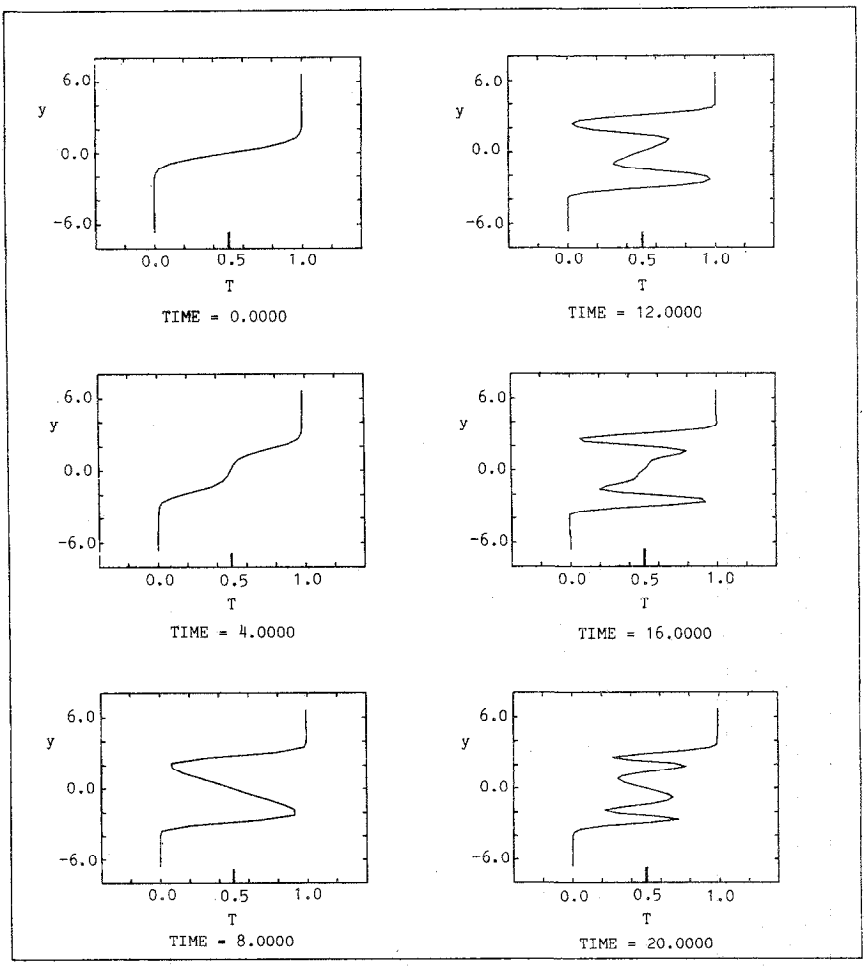

FIG. 20. The temperature distribution across the layer at the center of the core for λ^* and $\varepsilon/\lambda = 0.1$. The numerical parameters are the same as in Fig. 4.

$$\Upsilon = \int_0^{\lambda} \int_{-\infty}^{\infty} |T(\mathbf{x}, t) - \Theta(\mathbf{x})| \, d\mathbf{x}; \tag{22}$$

Υ can be regarded as an average thermal thickness of the shear layer. Within the linear range, the temperature distribution remains essentially the same, except for getting shifted up or down depending on the local sign of the perturbation. In Fig. 21, the natural logarithm of $\Upsilon(t)$ is shown for three values of the initial amplitude of the perturbation. The accuracy of the calculation of the temperature profiles depends on the initialization of the vorticity and temperature gradient and on the value of δ/h.

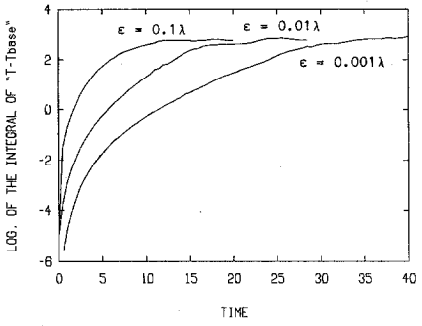

FIG. 21. The variation of the logarithm of the temperature thickness Y with time for the cases in Figs. 2, 3, and 4.

During the second stage, and with the rollup of the interface and the establishment of a spiral center at the midpoint of the wavelength, a complex temperature gradient develops as a result of the motion of the cold fluid upwards and the hot fluid downwards around the spiral center. Within this stage, if the number of transport elements remained the same, i.e., stretch was not accomodated by introducing elements where the local strain is large, the temperature distribution would collapse very quickly. In the problem of periodic shear layer, this collapse leads to values of $T(x, +\infty, t) < 1$ and $T(x, -\infty, t) > 0$. The reason of the loss of accuracy is clear from Eq. (16). When the elements move apart, the accuracy of computing the velocity gradient $\nabla \mathbf{u}$ deteriorates, and hence the new values of $\mathbf{q}_i$ accumulate large errors. Thus, while the calculation of the velocity field at the early stages of strong stretch using a fixed number of vortex elements may be acceptable for a short period of time, the calculations of the velocity gradient and the evolution of a passive scalar will show unacceptable errors.

To continue beyond the linear stage, the distance between neighboring elements in the principal direction of strain, $\Delta\chi$, must be monitored. If $\Delta\chi > \beta h$, where $\beta > 1$, one extra element is added between the two original elements and the total value of $\mathbf{q}_i$ is redistributed equally between the three elements. In the calculations, we used $\beta = 1.5$. Numerical convergence, in which one systematically refines the numerical parameters until no more changes are observed, was used to obtain these results.

The effect of the shear layer rollup on the temperature distribution is seen in Figs. 18 and 19. Immediately after the interface reaches a vertical position, an S-shape starts to form indicating that cold fluid has been transported from the lower stream into the upper stream and vice versa. This phenomenon, known physically as engulfment or entrainment, relies solely on convective transport and is observed when molecular diffusion, which acts to dissipate the sharp gradients, is small. Fast entrainment with small diffusion leads to "unmixedness" of hot and cold fluids within the eddy core. With more fluid being transported to the opposite stream the S-shape grows, reaching a maximum amplitude when the interface becomes horizontal. At this moment, fluid with the maximum and the minimum

temperature has been entrained into the core, i.e., entrainment has reached all the way to the free streams to bring fluid into the core of the eddy. This is the stage of maximum entrainment when the core size reaches its largest size and cannot accommodate any more fluid. In the case of $\varepsilon = 0.1\lambda$, it corresponds to $t = 8.0$, which is at the end of the second stage of development. To make the correspondence between the temperature profiles and the evolution of the interface of the layer clear, we plot the latter in Fig. 22, showing the actual vortex elements that were used in the computations of the interface. At this time, the interface has rotated 180° around the spiral center. This is the first step in the process of homogenization of the core.

As the core rotates further into the third stage, the inner part of the interface develops a secondary instability that rolls up in a very similar manner to the primary instability. This secondary instability is in phase with the primary instability and can be envisioned by zooming in on the intersection between the interface and the horizontal centerline of the layer. Due to the elongation of the outside envelope of the core, the wavelength of the secondary instability grows with time, as seen from Fig. 22. However, the amount of fluid within the elliptical

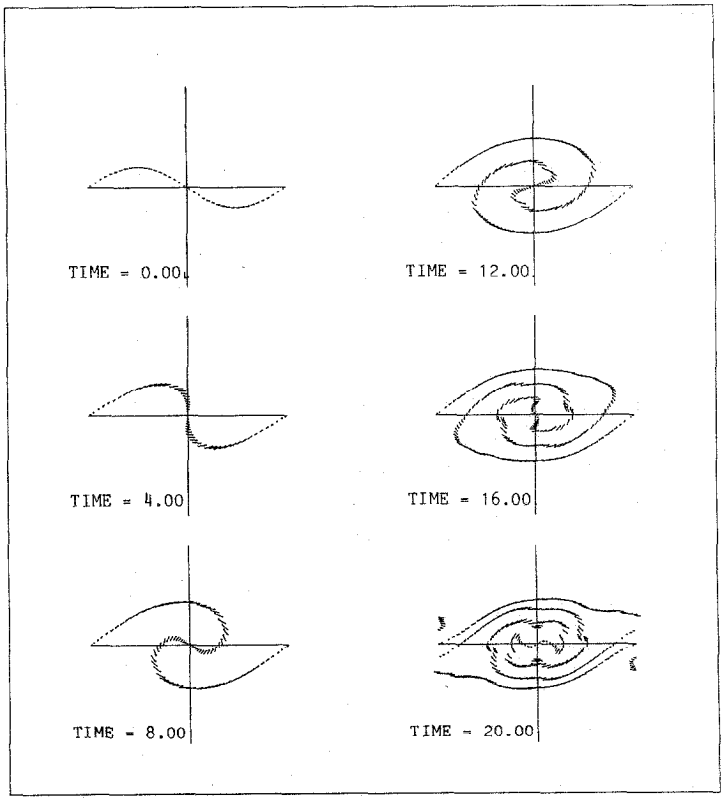

FIG. 22. The rollup of the interface, defined by the layer which coincides with $y = 0$ at $t = 0$ for the case shown in Fig. 4.

envelope remains constant, or decreases slowly as seen from Fig. 21 for the temperature thickness of the layer. The growth of the secondary instability provides a mechanism of internal entrainment within the core. During the growth of the secondary instability, an inverted S-shape, or a Z-shape, forms in the middle of the temperature profile, Figs. 18–20. The entrainment associated with this instability turns the fluid in a clockwise fashion, making the inside of the core more uniform. This is seen from the decay of the peaks in the temperature profile as this Z-shape grows.

With another 180° turn of the interface at the spiral center, a smaller S-shape forms in the middle of the profile due to the onset of an even shorter wavelength instability that is in-phase with the primary instability. While the existence of the secondary instability was not observed before in numerical simulations, its presence is clearly seen in the experimental results in Fig. 9.

The onset and subsequent growth of successively shorter wavelength instabilities continues, leading to a more uniform temperature distribution within the eddy core. An asymptotic limit to this process can be foreseen: it is the formation of a temperature profile with the following shape: $T = T_\infty$ at $y > \Delta/2$; $T = T_{-\infty}$ at $y < -\Delta/2$, and $T = (T_\infty + T_{-\infty})/2$ in between, where Δ is the minor axis of the elliptical envelope at $x = \lambda/2$. This shape has been measured experimentally by Konrad [32] (see also Broadwell and Breidenthal [33]), for mixing layer flows at high Reynolds numbers. This is, to our knowledge, the first time it has been computed numerically.

By the end of the third stage, the layer cannot absorb any more energy and a relaxation process occurs, during which the kinetic and thermal energy are fed back into the main flow streams. This reverse action is accompanied by the fluid leaving the core and moving back into the main streams at a very slow rate.

III.3. *Effect of Molecular Diffusion*

The generation of large temperature gradients within the core as successive instabilities evolve gives rise to large molecular diffusion fluxes which act to smooth

is very small relative to the convective transport, i.e., the Reynolds number is high, diffusion plays an important role since mixing at the molecular scales can only be accomplished via molecular diffusion. Thus, the combined action of convective entrainment and molecular diffusion leads to the homogenization of the temperature within the eddy core. To simulate the effect of diffusion for small values of α in the current model of a shear layer, Eqs. (15) and (16) are modified by adding a diffusion term,

$$\frac{\partial T}{\partial t} + \mathbf{u} \cdot \nabla T = \alpha \nabla^2 T \tag{23}$$

and

$$\frac{\partial \mathbf{q}}{\partial t} + \mathbf{u} \cdot \nabla \mathbf{q} = -\mathbf{q} \cdot \nabla \mathbf{u} - \mathbf{q} \times \omega + \alpha \nabla^2 \mathbf{q}, \tag{24}$$

where α is the nondimensional molecular diffusivity, or the inverse of the Peclet number. At high speed flow, the Peclet number is typically $10^3 - 10^5$. To solve Eq. (24) using the scheme that we have developed, a third fractional step must be added, in which the value of $\mathbf{q}$ is updated according to

$$\frac{\partial \mathbf{q}_i}{\partial t} = \alpha \nabla^2 \mathbf{q}_i \tag{25}$$

without changing the shape of the core function or the value of $\mathbf{q}_i$. By taking $\delta = \delta(t)$, and substituting Eq. (19) into Eq. (25), we find that $d\delta^2/dt = 4\alpha$. Thus, the core radius must change according to

$$\delta^2 = \delta_0^2 + 4\alpha t, \tag{26}$$

where δ_0 is the core radius at $t = 0$ (for more discussion, see Leonard [1], Ashurst [34].) The cores of the vortex elements and of the temperature gradient elements become different with time.

Results in Fig. 23 show the temperature profile at $T = 20$ for the case of λ^* and $\varepsilon = 0.1\lambda^*$, evaluated for $\alpha = 0.0$, 0.00001, 0.0001, 0.001, 0.01, and 0.1. Note that the temperature profiles of the first two cases are almost identical, indicating that the effective diffusivity of the inviscid calculation is of the order of 10^{-5}. In the last case, the temperature profile is similar to the case of pure diffusion, indicating that diffusion proceeds at a rate faster than the instability. It is also noticed that for moderate values of α, $0.0001 < \alpha < 0.01$, diffusion only affects the core of the eddies, making them achieve a homogeneous state faster.

Greengard [35], in his analysis of the core-spreading vortex method in which a fixed number of elements are used to perform the convective transport and their cores are expanded to account for the effect of diffusion, showed that the scheme does not converge to the correct equation of motion except when the flow field outside the region $|\omega| > 0$ is uniform. We have used a core spreading scheme to simulate the effect of diffusion in the energy equation with two modifications: (1) the number of transport elements which discretize the gradient field is increasing with time; and (2) α is kept small. Utilizing an increasing number of elements to perform the convective transport is essential since it is important to determine the gradient field accurately, in terms of the location and strength of the elements, before the diffusion effect can be added. In essence, adding transport elements at areas of high strain allows the computational elements to capture all the vorticity and temperature gradient carrying fluid at all times, even after the vorticity has been fragmented by the action of the strain field. Without this step, strain will create areas which are void of elements, thus, diffusion cannot be represented.

In the particular application of a shear layer at high Reynolds number, the flow field is uniform outside the area where $|\omega| > 0$, and this area expands slowly by diffusion if $\alpha < 1$. Limiting the simulations to small values of α: (1) reduces the errors associated with the fractional step scheme used to solve Eq. (24) (Beale and

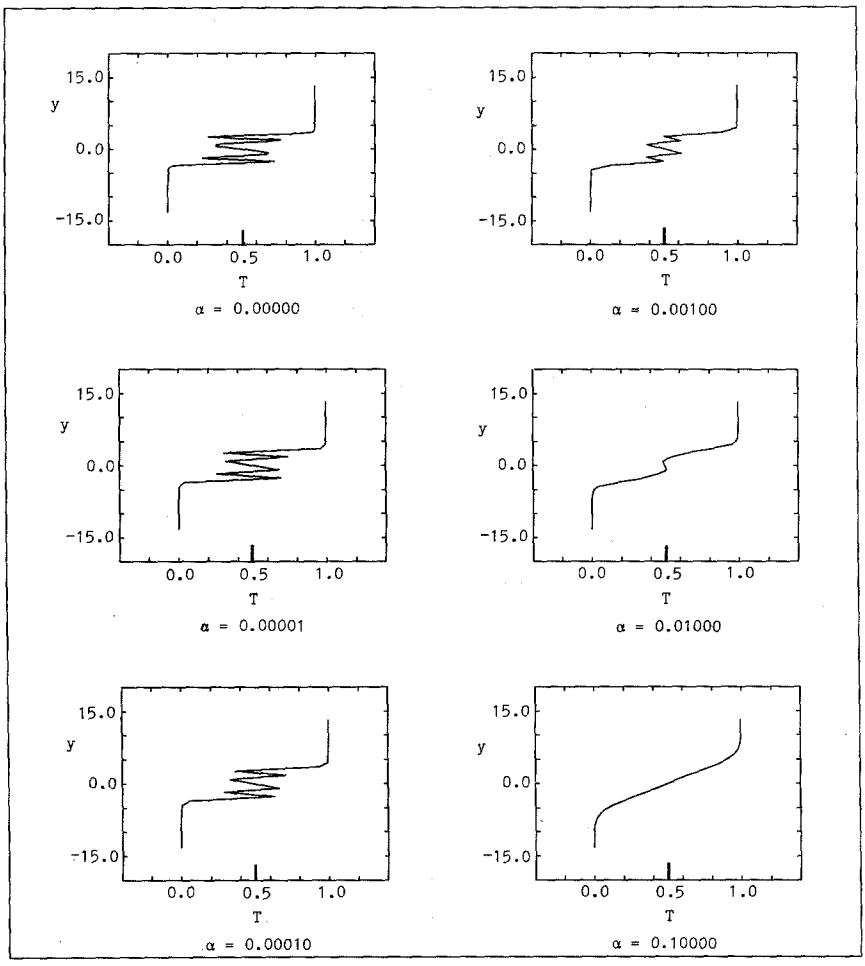

FIG. 23. The effect of thermal diffusion on the temperature distribution across the layer. Temperature is shown at $t = 20$ for the case shown in Fig. 4.

Majda [36]); and (2) reduces the errors concomitant with convecting an element with the velocity evaluated at its center while its core radius is growing. To accommodate this growth, which causes the spread of vorticity in the direction normal to the streamlines, one may be forced to add elements in the direction normal to the maximum principal strain direction and then redistribute the vorticity. It is, therefore, clear that the scheme is only applicable when $\alpha < 1$ and for short time, i.e., $\alpha t < 1$. If these two conditions are not satisfied, one must divide each element whose core radius is larger than a critical value into a number of separate elements so that the convective transport can be performed accurately. Since most interest in shear layer flows is at high Reynolds number, or $\alpha < 1$, and within the short time of

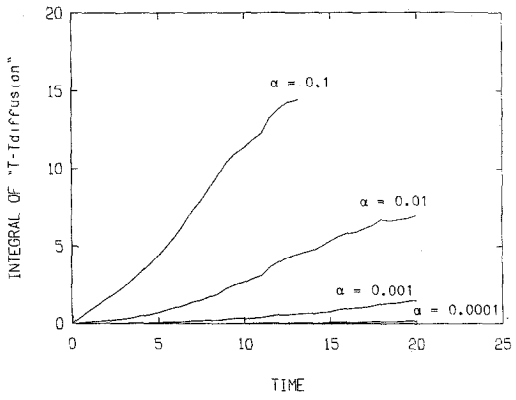

Fig. 24. Total mixing, $M(t, \alpha, 0.1)$ due to the combined action of entrainment and diffusion, evaluated for different values of α.

development of the convective instability, we feel that the current scheme is sufficient for this application.

To define a quantitative measure of mixing in a single phase fluid with thermal stratification, we observe first that mixing is only achieved by molecular diffusion. Large entrainment fluxes bring the unmixed fluid layers in contact along a larger interface; however, molecular diffusion across this interface is what accomplishes the actual mixing. A measure of mixing can be defined as

$$M(t, \alpha, \varepsilon) = \int_0^{\lambda} \int_{-\infty}^{\infty} |T(\mathbf{x}, t, \alpha, \varepsilon) - T(\mathbf{x}, t, 0, \varepsilon)| \, d\mathbf{x}.$$

Note that $M(t, 0, \varepsilon) = 0$, while $M(t, \alpha, 0)$ is due to diffusion only. In Fig. 24 $M(t, \alpha, 0.1)$ is plotted for various values of α and for λ^*. It represents mixing due to the combined action of entrainment and diffusion. At very small values of α, mixing is limited by the amount of diffusion across the fluid layers which have been entrained into the eddy core. Since for these values of α the convective transport is faster than the diffusive transport, mixing increases approximately as $\sqrt{\alpha}$. However, as α increases, and at longer times, mixing proceeds at a slower rate since it becomes bounded by entrainment of unmixed fluid into the eddy core which almost ceases by the end of the second stage of rollup.

IV. Conclusions

In this work, the vortex element method is used to compute both the early and late stages of development of an inviscid temporal mixing layer. In this method, the vorticity is initially discretized among overlapping elements of radially symmetric cores. We find that using a scheme which depends on equating the vorticity at the centers of the elements with the accumulative value induced by all elements is

necessary to obtain accurate results for initial vorticity discrezation. We also find that to ensure the accuracy of the solution for short times, the ratio of the core/separation should be larger that one. Very large cores introduce a strong perturbation in the vorticity field, while smaller cores cause a fast deterioration of accuracy. Using fourth-order Gaussian cores results in better accuracy over second-order Gaussian cores. However, we feel that the improvement in accuracy does not

values due to the generation of strong stretch. This leads to the computation of inaccurate velocities and is manifested by the irregular motion of the vortex elements. To overcome this problem, the vorticity is constantly redistributed among elements inserted along the principal direction of strain to capture the local deformation of the vorticity field and to improve the resolution of the calculations. This is achieved by an insertion-and-interpolation process, which is applied where the distance between the neighboring centers along the principal direction of strain exceeds a threshold value. We show, using solutions for a shear layer perturbed at different wavelengths and amplitudes, that this process yields accurate solutions for the vorticity distribution at long times and after strong strain fields have caused a severe distortion of the streamlines. This scheme enables one to accurately compute the local velocity gradient which, while it is not required in connection with vorticity convection, is necessary for the accurate evaluation of the convection of a passive scalar.

The temperature gradients, distributed over transport elements which resemble in their structures the vortex elements, are used to compute the temperature distribution as the rollup evolves. Contrary to vorticity, scalar gradients are not conserved along particle paths, thus, the strength of these transport elements is changed according to the straining and rotation of the material elements. The scheme is capable of capturing very sharp gradients that develop within the core since the elements migrate towards these zones by convection. The multiplication of these elements via stretch, which inadvertently mimics the physical process by which large scalar gradients are generated, provides a naturally adaptive grid to compute these gradients. By expanding the cores of the transport elements, the effect of small diffusivities can be simulated as a small perturbation to the convection field. Diffusion, even at high Peclet number, is responsible for generating areas of uniform temperature inside the eddy since it acts to smooth out the sharp gradient created by convection.

The application of vortex methods to problems in which the no-slip boundary condition along solid walls must be satisfied can be accomplished using the random vortex method (Chorin [37], and Sethian and Ghoniem [38].) In this method, extra vortex elements are generated along the solid walls to cancel the slip velocity, and the diffusion of vorticity is simulated by the random walk of the vortex elements. At high Reynolds number, a strong strain field is expected to cause similar problems as described in this work, i.e., areas of large stretch will be depleted from vortex elements and accurate resolution of the vorticity field may be

lost around these areas. Extending the insertion-and-interpolation scheme described in this work to the random vortex method requires: (1) adding a third fractional step, which must be performed after the convection and before the diffusion steps, for the redistribution of the vorticity field among elements arranged in the direction of principal strain; and (2) computing the strain field at the center of the vortex elements in a Lagrangian form since, due to random walk, neighboring vortex elements and neighboring material elements change as time evolves. The implementation of these two steps must be preceded by careful formulation and will require lengthy computation.

REFERENCES

1. A. LEONARD, *J. Comput. Phys.* **37**, 289 (1980).
2. J. T. BEALE AND A. MAJDA, *J. Comput. Phys.* **58**, 188 (1985).
3. O. H. HALD, *SIAM J. Num. Anal.*, in press.
4. A. F. GHONIEM AND K. K. NG, *Phys. Fluids* **30**, 706 (1987).
5. A. J. CHORIN, *J. Fluid Mech.* **57**, 785 (1973).
6. M. J. FRITTS AND J. P. BORIS, *J. Comput. Phys.* **31**, 173 (1979).
7. N. J. ZABUSKI, M. H. HUGHES, AND K. V. ROBERTS, *J. Comput. Phys.* **30**, 96 (1979).
8. A. J. CHORIN, T. J. R. HUGHES, M. F. MCCRACKEN, AND J. E. MARSDEN, *Commun. Pure Appl. Math.* **41**, 205 (1978).
9. V. M. DEL-PRETE AND O. HALD, *Math. Comput.* **32**, 791 (1978).
10. O. H. HALD, *SIAM J. Num. Anal.* **16**, 726 (1979).
11. T. J. BEALE AND A. MAJDA, *Math. Comput.* **39**, 1 (1982).
12. T. J. BEALE AND A. MAJDA, *Math. Comput.* **39**, 29 (1982).
13. Y. NAKAMURA, A. LEONARD, AND P. SPALART, *Proceedings, AIAA/ASME Third Joint Thermophysics, Fluids, Plasma and Heat Transfer Conference*, AIAA Paper 82-0948, 1982.
14. S. ROBERTS, *J. Comput. Phys.* **58**, 29 (1985).
15. M. PERLMAN, *J. Comput. Phys.* **59**, 200 (1985).
16. C. ANDERSON AND C. GREENGARD, *SIAM J. Num. Anal.* **22**, 413 (1985).
17. C. ANDERSON, *J. Comput. Phys.* **61**, 417 (1985).
18. R. KRASNY, *J. Comput. Phys.* **65**, 292 (1986).
19. N. J. ZABUSKI AND E. A. OVERMAN, *J. Comput. Phys.* **52**, 35 (1983).
20. R. KRASNY, Computation of vortex sheet rollup in the Treffetz plane, submitted for publication.
21. A. J. CHORIN, in *Computing Methods in Applied Sciences and Engineering*, edited by R. Glowinski and J. L. Lions (North-Holland, INRIA, Amsterdam, 1980), p. 229.
22. A. F. GHONIEM AND A. K. OPPENHEIM, in *Proceedings, 8th Int. Conf. Num. Methods Fluid Dynamics*, edited by E. Krause (Springer-Verlag, New York, 1982), p. 224.
23. A. F. GHONIEM AND A. K. OPPENHEIM, *AIAA J.* **22**, 1429 (1983).
24. A. F. GHONIEM AND F. S. SHERMAN, *J. Comput. Phys.* **61**, No. 1 (1985).
25. C. ANDERSON, Ph. D. dissertation, Department of Mathematics, U.C. Berkeley, 1983 (unpublished).
26. A. MICHALKE, *J. Fluid Mech.* **19**, 543 (1964).
27. R. BETCHOV AND N. O. CRIMINALE, JR., *Stabiliyy of Parallel Flows* (Academic Press, New York, 1967), p. 330.
28. G. M. CORCOS AND F. S. SHERMAN, *J. Fluid Mech.* **73**, 29 (1976).
29. F. A. ROBERTS, P. E. DIMOTAKIS, AND A. ROSHKO, in *Album of Fluid Motion*, edited by M. Van Dyke (Parabolic Press, Stanford, CA, 1982), p. 85.
30. C. POZRIKIDIS AND J. J. L. HIGDON, *J. Fluid Mech.* **157**, 225 (1985).

31. J. J. RILEY AND R. W. METCALFE, *Proceedings, AIAA 19th Aerospace Sciences Meeting*, AIAA Paper 80-0274, 1980.
32. J. H. KONRAD, Project SQUID Tech. Rep. CIT-8-PUI, 1976 (unpublished).
33. J. E. BROADWELL AND R. E. BREIDENTHAL, *J. Fluid Mech.* **125**, 397 (1982).
34. W. T. ASHURST, in *Proceedings, 1st Symposium on Turbulent Shear Flow*, edited by Durst *et al.* (Springer-Verlag, Berlin, 1979), p. 402.
35. C. GREENGARD, *J. Comput. Phys.* **61**, 345 (1985).
36. J. T. BEALE AND A. MAJDA, *Math. Comput.* **37**, 243 (1981).
37. A. J. CHORIN, *SIAM J. Sci. Statist. Comput.* **1**, 1 (1980).
38. J. A. SETHIAN AND A. F. GHONIEM, *J. Comput. Phys.* **74**, 283 (1988).